Mineralogical Magazine, February 2016, Vol. 80(1), pp. 143–156

Structural anomalies in tobelite-2M_2 explained by high resolution and analytical electron microscopy

G. C. Capitani[1], E. Schingaro[2,*], M. Lacalamita[2], E. Mesto[2] and F. Scordari[2]

[1] Dipartimento di Scienze dell'Ambiente e del Territorio e di Scienze della Terra, Università di Milano Bicocca, P.za della Scienza 4, I-20126 Milano, Italy

[2] Dipartimento di Scienze della Terra e Geoambientali, Università degli Studi di Bari ALDO MORO, via E. Orabona 4, I-70125 Bari, Italy

[*Received 23 November 2014; Accepted 19 May 2015; Associate Editor: M. Welch*]

ABSTRACT

A transmission electron microscopy (TEM) investigation was undertaken in order to elucidate the nature of the structural disorder in a tobelite specimen from the sedimentary rocks of the Armorican sandstones (western France). This structural disorder may be the origin of residual electron-density maxima in difference-Fourier maps reported previously in single-crystal XRD studies of tobelite. The TEM investigation of tobelite confirmed that it is the 2M_2 polytype in subfamily-B, but the ordered sequence is interrupted by numerous stacking faults parallel to (001), for which the stacking vectors belong to both subfamilies-A and -B of mica polytypes, with a prevalence of the latter. Chemical heterogeneity depending on the Si/Al ratio and Na and Mg concentration was observed at the nanoscale among different mica lamellae in a single crystal. The observed variations are consistent with a change in mica chemistry leading to interlayer vacancies which may cause shortening of the interlayer separation, as revealed by the single-crystal structure refinements.

Keywords: tobelite, 2M_2 polytype, electron microscopy, stacking disorder.

Introduction

Mica polytypism arises from the pseudo-hexagonal symmetry of the tetrahedral sheet for which, in principle, there are six different possible ways to stack successive T–O–T layers, each characterized by rotations between the adjacent layers around **c*** by different multiples of 60° (Nespolo, 1999; Ferraris and Ivaldi, 2002). Smith and Yoder (1956) derived the six standard polytypes (1M, 2M_1, 3T, 2M_2, 2O and 6H). Zvyagin (1988) then introduced the notion of 'homogeneous polytypes', which were defined as those polytypes whose successive layers are always related by the same angle, apart from the sign, as opposed to more complex polytypes, called 'inhomogeneous polytypes'. According to Nespolo (2001), in homogeneous polytypes the position of any layer relative to the others and the transition from it to the adjacent ones are the same or equivalent for all layers, giving rise to the standard polytypes of Smith and Yoder (1956). Inhomogeneous polytypes are those whose stacking sequence is based on that of the homogenous ones, broken up by periodic stacking faults. Most of the inhomogeneous polytypes belong to the 1M and 3T structural series, whereas those belonging to the 2M_1 structural series are rarer (Takeda and Ross, 1995). Finally, mica polytypes were grouped, on the basis of the equivalence of layer pairs (see also Backhaus and Ďurovič, 1984; Ďurovič *et al.*, 1984; Nespolo, 1999) into: (1) subfamily-A polytypes (1M, 2M_1 and 3T), which are characterized by $2n \times 60°$ rotations (n integer) between adjacent layers; (2) subfamily-B polytypes (2M_2, 2O and 6H), characterized by $(2n+1) \times 60°$ rotations between adjacent layers; and (3) mixed rotations polytypes characterized by operating vectors of

E-mail: emanuela.schingaro@uniba.it
DOI: 10.1180/minmag.2015.079.7.14

© 2016 The Mineralogical Society

https://doi.org/10.1180/minmag.2015.079.7.14 Published online by Cambridge University Press

both A and B subfamilies. Only homogeneous polytypes have been reported in subfamily B (Kogure and Nespolo, 1999*a*).

Subfamily-B, as well as mixed rotation polytypes, are much less abundant in nature than subfamily-A polytypes. This difference is due to the different atomic arrangement in the interlayer. In subfamily-B polytypes, basal tetrahedral oxygens on the adjacent layers are exactly superimposed along the **c*** direction. In subfamily-A polytypes, these basal oxygens are laterally displaced from each other due to ditrigonal distortion of the tetrahedral rings, thereby reducing the repulsive forces between the oxygens facing across the interlayer and making the structural configuration energetically more favorable (Ferraris and Ivaldi, 2002). Nonetheless, $2M_2$ polytypes have been reported for lepidolite (Levinson, 1953), illite (Shimoda, 1970), nanpingite (Ni and Hughes, 1996) and tobelite (Mesto *et al.*, 2012). The $2O$ polytype has been reported for anandite (Giuseppetti and Tadini, 1972) and phlogopite (Ferraris *et al.*, 2001). Mixed-rotation polytypes or stacking sequences where both $2n \times 60°$ and $(2n+1) \times 60°$ rotations occur (Nespolo, 1999), have also been reported for annite (Kogure and Nespolo, 1999*a*), oxybiotite (Kogure and Nespolo, 1999*b*), lepidolite (Kogure and Bunno, 2004), gümbelite (Kameda *et al.*, 2007) and celadonite (Kogure *et al.*, 2008).

Analysis of polytypism and/or polytypic disorder is particularly interesting for tobelite, a rare dioctahedral mica with ideal composition $(NH_4)Al_2(Si_3Al)O_{10}(OH)_2$, firstly found by Higashi (1982) in the Ohgidani pottery stone deposit at Tobe (Japan). Tobelite was found to be the $1M$ polytype (Higashi, 1982; Hovis *et al.*, 2004) and also to be a mixture of $1M$, $2M_1$, $2M_2$, $3T$ and $2O$ polytypes (Harlov *et al.*, 2001; Pöter *et al.*, 2007). Mesto *et al.* (2012) first published the results of the single-crystal structure refinement of tobelite and NH_4^+-rich muscovite from the sedimentary rocks of the Armorican sandstones, western France. The analysed crystals have two peculiar features: (1) they belong to $2M_2$ polytype; (2) they exhibit unusual structural disorder.

Structure refinements of $2M_2$ mica polytypes are very rare in the literature and are limited to dioctahedral mica (Zhoukhlistov *et al.*, 1973), nanpingite (Ni and Hughes, 1996) and tobelite (Mesto *et al.*, 2012). This paucity of data is probably related both to the rarity of this mica polytype in nature and to the abundant stacking disorder, widespread in micas and particularly pronounced in tobelite. In tobelite and NH_4^+-rich muscovite from Armorican sandstones two kinds of disorder were found from the X-ray structure analysis. One is the classical stacking disorder as evidenced by the presence of streaks along the **c*** direction in the *h*0*l*, 0*kl* and higher levels calculated precession images. The other kind of disorder shows up as systematic residual electron densities of $\sim 2\ e^-/Å^3$ around the M2, T1 and T2 sites (Mesto *et al.*, 2012). They are distributed in the structure as pairs parallel to the [001] direction and located symmetrically with respect to the sites of the structure at a distance of 0.6 Å. During structure refinement of the NH_4^+-rich muscovite, such disorder was modelled with the introduction of TOT sheets which could undergo a rigid $\pm z$ translation across the interlayer site. A tentative interpretation of the residual electron densities pointed to the existence of a second minor structural component in the NH_4^+-rich muscovite crystal, with a c parameter shortened by $\sim$1.32 Å (i.e. having $c \approx 19.30$ Å) with respect to the dominant $2M_2$ structure with $c = 20.616(3)$ Å (Mesto *et al.*, 2012).

The characterization of stacking sequences in mica can be studied using high-resolution transmission electron microscopy (HRTEM) (e.g., Kogure, 2002; Fregola *et al.*, 2009 and reference therein). The present HRTEM investigation has been undertaken on tobelite-$2M_2$ from the same suite of samples studied by Mesto *et al.* (2012). Investigation on such a peculiar mica was carried out in order to gain insights into the nature of the structural disorder in the tobelite-$2M_2$, as suggested by X-ray structure analysis (Mesto *et al.*, 2012). The interest for this mineral phase also stems from tobelite and NH_4^+-rich muscovite being recognized as a potential long-term reservoir of nitrogen (as NH_4^+) in the deep Earth and as a marker of ancient biological activity (Busigny and Bebout, 2013). Their occurrence may be used as fingerprints in oil exploration and also have thermobarometric implications (Ruiz Cruiz, 2011 and references therein).

Occurrence

A detailed description of the geological setting in which the studied micas occurred was reported by Gloaguen *et al.* (2007) and Tartese *et al.* (2014) and is briefly summarized here. Tobelite was found in Lower Ordovician oolitic ironstone of the Saint-Aubin-des-Châteaux quarry (Armorican massif, Hercynian belt of western France). This deposit

https://doi.org/10.1180/minmag.2015.079.7.14 Published online by Cambridge University Press

underwent epigenetic transformation of the organic rich ore by successive hydrothermal fluid pulses. Specifically, the process consisted of three main stages: massive sulfidation (Stage 1); fracturing with consequent base-metals deposition in veins (Stage 2); formation of Pb-Sb-Au paragenesis in veins (Stage 3). At Stage 3, the paragenetic sequence contains tobelite (referred to as 'white mica'), quartz, chamosite, tourmaline, late galena, chalcopyrite, pyrite, Sb-sulfosalts (bournonite, boulangerite and tetrahedrite) and electrum. The thickness of tobelite veins is between 0.5 to 10 cm. Typical tobelite vein infill starts with a rim of green chlorite. This is followed by quartz including tobelite 'rosettes'. Between quartz crystals the sulfide paragenesis could be observed (Gloaguen, personal communication). On the basis of the chamosite geothermometer, the closure temperature was calculated as 275 ± 9°C for the Stage 3 paragenesis (Gloaguen *et al.*, 2007).

Experimental

Cross sections of tobelite were prepared by mixing tobelite crystal fragments (up to 1 cm in size), notably flattened on (001) as common to mica minerals, with epoxy resin. The mixture was then squeezed between two glass slides before hardening, causing the (001) faces to dispose parallel to the glass slides. The slides with their mica filling were cross-sectioned, mechanically thinned down to 30 μm and polished on both sides (Kogure, 2002, 2013). At this step of the sample preparation, the specimen was investigated by X-ray energy dispersive spectrometry using a scanning electron microscope and energy dispersive spectroscopy (SEM-EDS) in order to check the mineral composition and the elemental distribution along the stacking of the mica. Electron transparency for transmission electron microscopy (TEM) observations was then achieved by argon ion-milling at a low angle with a Gatan PIPS. The samples were coated with carbon in order to avoid electrostatic charging during observation.

Qualitative compositional profiles (linescans) along the stacking sequence of the mica samples were performed at the Dipartimento di Scienze dell'Ambiente e del Territorio e di Scienze della Terra of the Milano-Bicocca University with a SEM Tescan VEGA TS 5136XM equipped with an EDAX EDS spectrometer. Linescans were measured at 20 keV, with step distance of ~15 nm and acquisition time to 200 ms.

The TEM investigations were performed at the Dipartimento di Scienze della Terra e Geoambientali of the University of Bari, and at the Dipartimento di Scienze Fisiche, della Terra e dell'Ambiente, of the University of Siena, by using two analogous JEOL-JEM 2010 microscopes with the following characteristics: operating voltage 200 kV, LaB_6 source, nominal point resolution of ~2.0 Å, spherical aberration of 0.5 mm; a double-tilt specimen holder (±20°) was used in both cases.

Microanalyses were obtained with a Link energy-dispersive X-ray (EDX) spectrometer and quantified following the Cliff-Lorimer approximation (Cliff and Lorimer, 1975), using theoretical K-factors. Aware of the quick diffusion of alkali and ammonium upon high-energy electron irradiation, we limited the electron dose on the analysed areas, and thus the elemental diffusion during acquisition, by spreading the beam up to a spot size diameter of ~100 nm. Live times of 50 s were used for semi-quantitative TEM-EDS analyses.

Images were recorded on either a Gatan MSC794 CCD camera (Bari) or on Fuji image plates (Siena) or photographic films (Siena). To remove noise contrast from amorphous materials, HRTEM images were either filtered rotationally (Kilaas, 1998) with the HRTEM filter (Mitchell, 2007), as implemented in the Gatan Digital Micrograph version 3.9 software, or filtered applying proper masks on the Fast Fourier Transforms (FFT) of the image in order to retain only the periodic signal, and then computing the Inverse Fourier Transform (IFT).

Results

Theoretical backgrounds

The $2M_2$ stacking is characterized by alternating ±60° rotations of the TOT layers. Within each TOT layer the upper tetrahedral ring is displaced by $b/3$ with respect to the lower tetrahedral ring when projected on the (001) plane, as for any other polytype (in subfamily-A polytypes the shift is $a/3$ because **a** and **b** axes exchange mutually). When the stacking sequence of a perfectly ordered tobelite-$2M_2$ is observed, for instance, along the [110] direction, and the operating vectors are assumed to be 2 and 3 (Fig. 1*a*), the sequence appears roughly as alternating 0 and $a/6$ shifts on the (310) plane. The same ordered sequence, when observed along the [130] direction, which is at ~30° from the [110] one, appears as a zig-zag sequence with alternating shifts on (110) of roughly $\pm b/6$. Any departure from these sequences entails

https://doi.org/10.1180/minmag.2015.079.7.14 Published online by Cambridge University Press

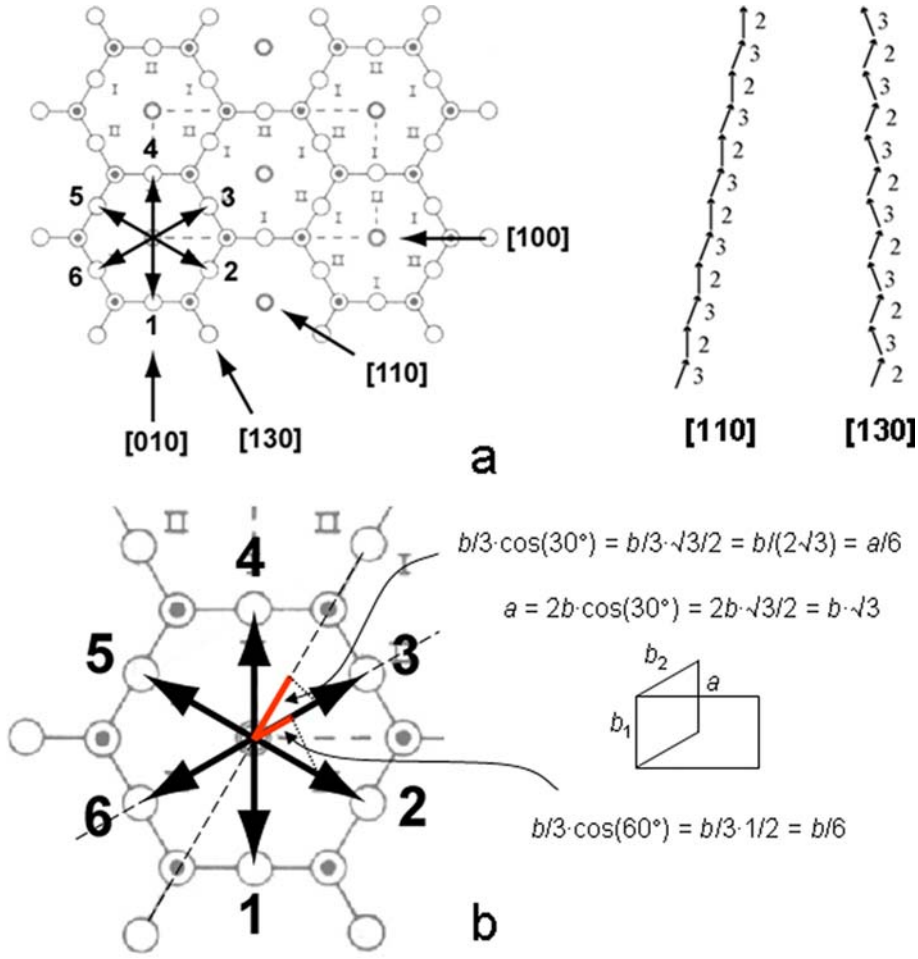


FIG. 1. (*a*) Schematic (001) projection of the tobelite structure (left) along with the six possible stacking vectors (modified from Kogure, 2002) and the stacking sequence observable in cross section along [110] and [130], respectively, for a perfectly ordered $2M_2$ structure (right). (*b*) Lateral shifts (red) observable in cross section for different observation directions and operating stacking vectors. From this figure we derive the lateral shifts observable on HR images along specific directions as a function of different operating stacking vectors, as reported on Table 1. Note that for a proper derivation of the shifts, one has to take into account the $a \approx b \cdot \sqrt{3}$ relationship due to the pseudo-hexagonal symmetry of micas and that a $b/3$ shift in one direction, because of the $b/2$ periodicity due to the $C2/c$ space group, corresponds to a $-b/3$ shift in the opposite direction ($b/3 + b/2 = 5b/6 = -b/6$).

the presence of stacking faults and, in principle, the full stacking sequence can be reconstructed by combining observations along these two directions. The full set of structural shifts due to one of the six possible stacking vectors for the principal observation directions perpendicular to **c*** can be retrieved from Fig. 1*b* and are presented in Table 1. They offer the rationale for the derivation of the stacking sequence on HR images whenever two independent directions are accessible.

In spite of the limitation deriving from the beam damage to the sample (see below), disorder affecting the diffraction intensity distribution, and the distortion usually accompanying HR images and selected area electron diffraction (SAED) patterns (e.g. Capitani *et al.*, 2006; Mugnaioli *et al.*, 2009), the whole set of diffraction patterns acquired were indexed successfully, within the experimental error, using the cell parameters for the $2M_2$ polytype refined by Mesto *et al.* (2012):

https://doi.org/10.1180/minmag.2015.079.7.14 Published online by Cambridge University Press

TABLE 1. Lateral shifts observable in tobelite along specific directions as a function of the different possible operating stacking vectors.

	1	2	3	4	5	6
[010]	0	*a*/6	*a*/6	0	–*a*/6	–*a*/6
[130]	*b*/6	–*b*/6	–*b*/3 (*b*/6)	–*b*/6	*b*/6	*b*/3 (–*b*/6)
[110]	–*a*/6	0	*a*/6	*a*/6	0	–*a*/6
[100]	*b*/3 (–*b*/6)	*b*/6	–*b*/6	–*b*/3 (*b*/6)	–*b*/6	*b*/6

Note: the *b*/3 shift in one direction, because of the *b*/2 periodicity on HR images due to the centred *C*2/*c* S.G., corresponds to a *b*/6 shift in the opposite direction.

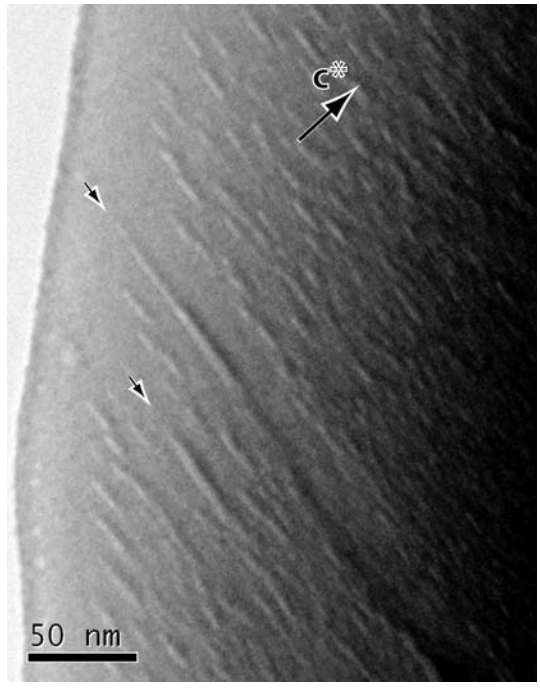


FIG. 2. Bright field image of tobelite showing lenticular features (arrowed) parallel to (001) produced by exposure to the electron beam.

$a = 9.03$, $b = 5.20$, $c = 20.62$ Å, $\beta = 100.1°$. The $2M_2$ stacking is thus confirmed and taken to be the primary polytype in the samples studied.

Radiation damage

Tobelite turned out to be very electron-beam-sensitive. After a few seconds of exposure, even at low magnification (i.e. low electron dose), lenticular features appeared parallel to (001) in bright-field images (Fig. 2), that look like microcleavage at higher magnification (see Fig. 3*a* and following high-resolution images). Similar features arising from beam damage have been reported for Na-bearing phyllosilicates such as kulkeite (Schreyer *et al.*, 1982), wonesite (Veblen 1983*a*, 1983*b*) and paragonite (Ahn *et al.*, 1986). Ahn *et al.* (1986) discuss the possible formation mechanism of the microcleavage in terms of diffusion of Na atoms. Diffusion of interlayer cations causes volume loss and, therefore, reduction of the basal

https://doi.org/10.1180/minmag.2015.079.7.14 Published online by Cambridge University Press

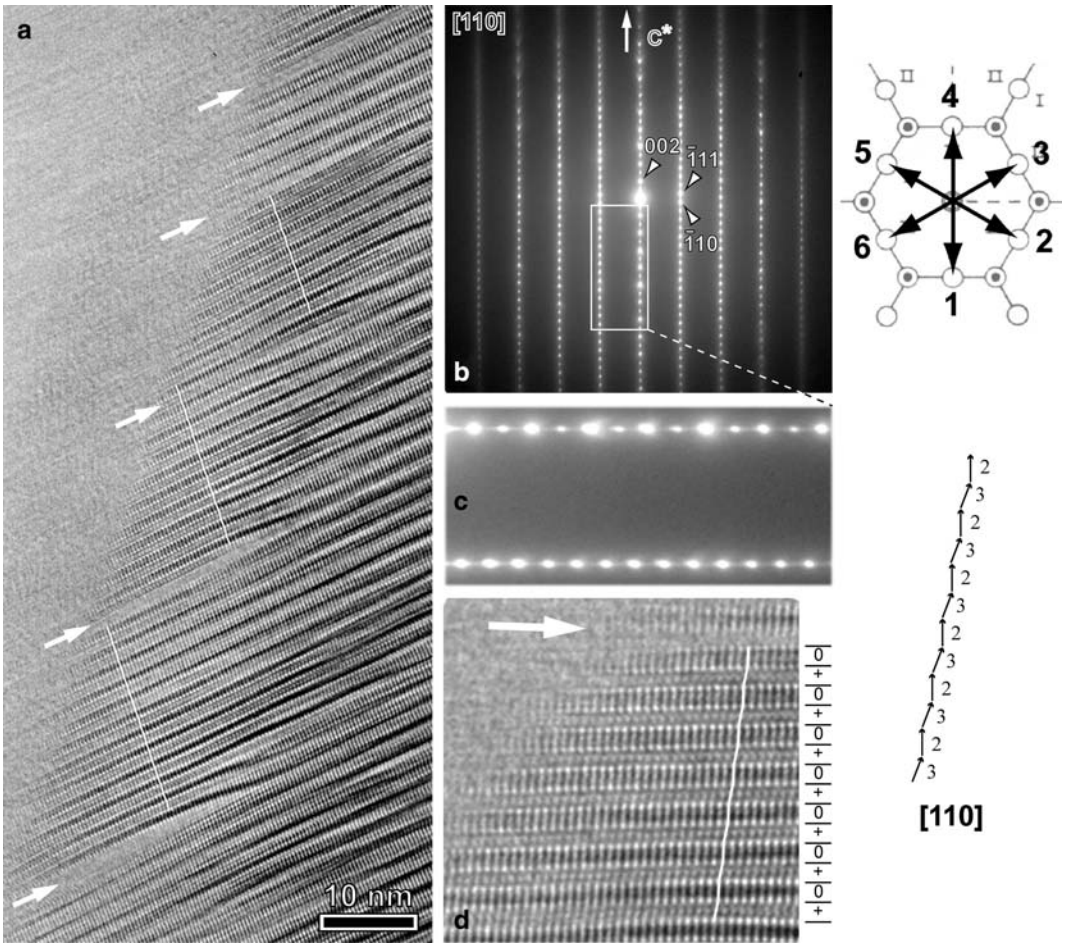


FIG. 3. High-resolution image of tobelite with [110] incidence (*a*) and corresponding SAED pattern (*b*). Note the incipient microcleavage produced by electron beam irradiation (white arrows). (*c*) Enlargement of the area indicated in (*b*). Note the bright background due to the inelastic scattering and the weak streaks along diffractions rows. (*d*) Enlargement of upper stacking sequence reported in (*a*). Assuming no subfamily A faults in this restricted area, the sequence should correspond to an ordered [32] sequence (lower right) characteristic of the tobelite-2M_2 structure. The '+' sign indicates an *a*/6 shift to the right (operating vector 3, upper right); the '0' sign indicates a 0 shift on the (310) plane (operating vector 2).

spacing. The release of the resulting elastic strain would eventually cause the mechanical separation of the (001) layers. A similar formation mechanism is suggested here for tobelite, assuming that in this case it is the diffusion of ammonium that causes the local collapse of the structure and the formation of microcleavage.

In spite of the beam sensitivity of tobelite, by using low electron doses it was possible to make instructive observations, even in high-resolution mode. In Fig. 3*a* an area of tobelite-2M_2 more than 100 nm wide was imaged viewing down [110]. In this image, homogeneous sequences are intercalated with beam-damaged areas. The corresponding electron diffraction pattern appears diffuse due to the amorphous material formed by beam damage (increasing towards the central beam, Fig. 3*b*) and the rows of reflections appear slightly streaked owing to the incipient parting of the interlayer (Fig. 3*c*). However, the 2-layer periodicity characteristic of tobelite-2M_2 can be seen in diffraction patterns from the markedly stronger 00*l*, *l* = even

https://doi.org/10.1180/minmag.2015.079.7.14 Published online by Cambridge University Press

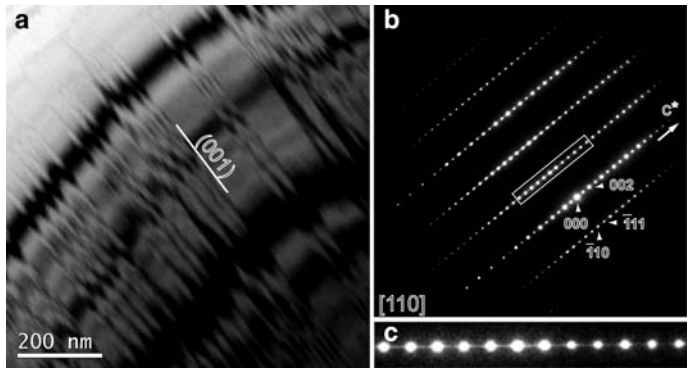


FIG. 4. (*a*) Bright field image of tobelite showing the high density of stacking faults parallel to (001). (*b*) Diffraction pattern of the [110] zone taken over the faulted area. Note the continuous streaking along ⟨11*l*⟩* rows (*c*).

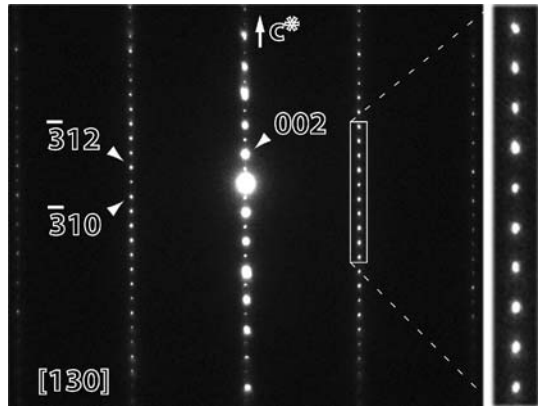


FIG. 5. Diffraction pattern taken along [130]. No streaks are evident along ⟨31*l*⟩* rows.

reflections as compared to the 00*l*, *l* = odd reflections. The latter, that should be absent because of symmetry, appear because of the dynamical scattering conditions. Furthermore, even if the structure images are heavily damaged by electron beam irradiation, the stacking sequences can be deduced from HR images (Fig. 3*d*). Assuming that no stacking vectors of subfamily-A are present, which may have the same projection on (310), the sequence can be indexed as a perfectly ordered 2M_2. However, as detailed below, the assumption of no subfamily-A faults does not completely hold.

Analysis of the stacking faults

Wide regions of polytypically-ordered structure are rare in the Armorican tobelite crystals. More frequently, a low magnification investigation of tobelite reveals many stacking faults parallel to (001), that appear as close bands that offset thickness fringes (Fig. 4*a*). A diffraction pattern of the [110] zone acquired from the faulted area (Fig. 4*b*) shows continuous streaking along *hkl* rows (Fig. 4*c*). On the other hand, all the diffraction patterns taken along [130] show no streaks along ⟨31*l*⟩* (Fig. 5). This observation should imply an absence of stacking vectors with mutual rotations of 0° or 120° in tobelite or, at least, that the occurrence of subfamily A faults is less than those of the subfamily B and below the detection limit for SAED experiments.

Observation along the [110] zone

In spite of the incipient beam damage that has locally altered the structure causing the bending of the layers, observation along [110] provided near

https://doi.org/10.1180/minmag.2015.079.7.14 Published online by Cambridge University Press

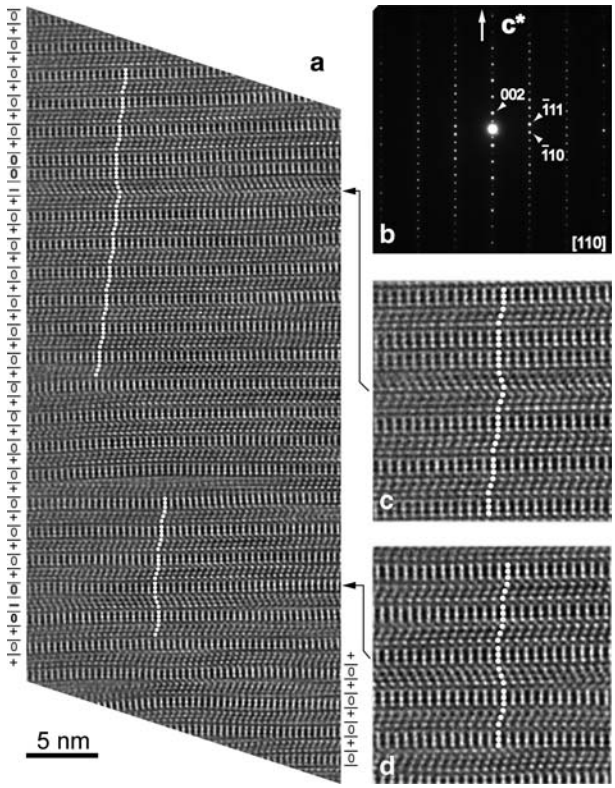


FIG. 6. [110] High-resolution image showing a crystal with a faulted $2M_2$ sequence (*a*), and corresponding SAED pattern (*b*). In (*c*) the ordered 0, +*a*/6 sequence is interrupted by a stacking fault which appears as a 180° rotation (subfamily B fault). The same projected shift of –*a*/6 can be produced, however, by a subfamily A rotation of –120°. The subsequent layer shows a 0 shift consistent either with a 0° (subfamily A fault) or 180° rotation; in (*d*) the ordered sequence is interrupted by a shift consistent either with a –60° (subfamily B fault) or a –120° rotation.

atomic resolution images of the stacking sequences (Fig. 6*a*; related diffraction pattern in Fig. 6*b*). Several faults with different stacking vectors were detected along this direction. In Fig. 6*c* it is apparent that the ordered 0, +*a*/6 sequence is interrupted by a stacking fault showing up as a 180° rotation, that is a shift according to vector [6]. However, the same projected shift of –*a*/6 can be produced by a subfamily A rotation of −120° (vector [1]). Then, the subsequent layer shows a 0 shift, which is consistent with a 0° or 180° rotation. In Fig. 6*d*, the ordered sequence is interrupted by a shift consistent either with a −60° (vector [1]) or a −120° (vector [6]) rotation. Other examples of ordered and disordered stacking sequences in the Armorican tobelite are reported in Fig. 7. Here, faults involving 0° (subfamily A) or 180° (subfamily B) rotations are present, but in this case the actual operating vector cannot be discriminated.

Observation along the [130] zone

As explained above, in order to reconstruct the complete stacking sequence of tobelite, a second structural image along [130] or [100] is necessary. This could not be achieved in tobelite as the structure became damaged after the first exposure along [110]. Even [130] HR images of unexposed areas resulted into poor quality images because of the higher resolution required. For these reasons, a complete reconstruction of the stacking sequence at the faulted regions was not possible.

In order to ascertain the presence of subfamily A faults in the samples studied, we investigated tobelite close to the [130] direction on lamellae not exposed previously to the electron beam and at lower magnification, in order to minimize the electron dose. Iijama and Buseck (1978) showed that in mica, when the crystal is slightly tilted away from the exact zone axis orientation, stacking faults

https://doi.org/10.1180/minmag.2015.079.7.14 Published online by Cambridge University Press

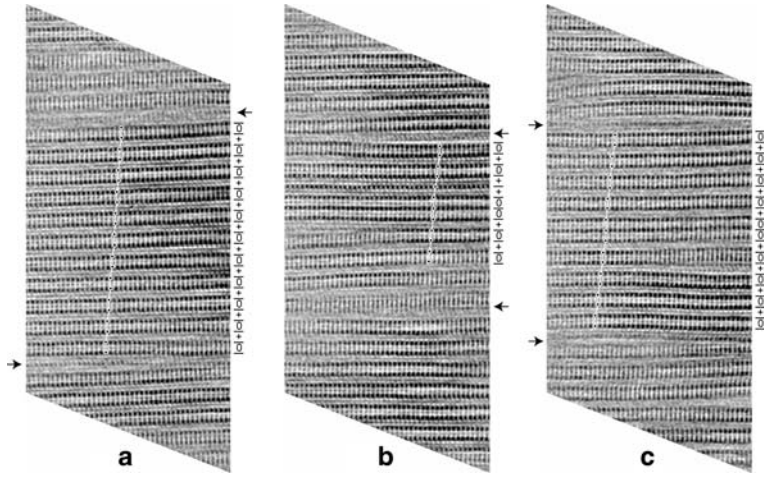


FIG. 7. [110] High-resolution images showing ordered (*a*) and disordered (*b* and *c*) sequences between highly damaged zones (arrows). The disordered sequences are affected by 0 and 180° rotations, but also in this case the actual operating vector can not be distinguished.

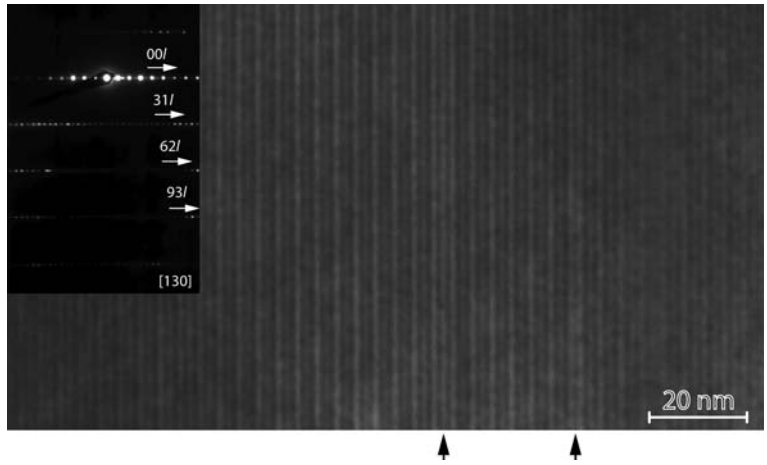


FIG. 8. Lattice fringes image taken slightly off the [130] direction and related diffraction pattern (inset). A two layer periodicity (~20 Å) is evidenced by alternating thin and thick bright fringes. The sequence is broken off by three and two adjoining bright mass-thickness contrast lamellae indicated by the black arrows. These are evidence of subfamily A faults.

with vector components perpendicular to the zone axis can be seen as changes in the periodicity along the stacking sequence in lower-magnification lattice-fringe images. In keeping with these authors, we acquired lattice fringe images of tobelite slightly off the exact [130] zone axis (Fig. 8). The corresponding diffraction pattern, documenting the misalignment, is displayed in the inset. A 2-layer periodicity, evidenced by alternating thick and thin brighter vertical fringes, is clearly recognized. The ordered sequence, however, is broken off by the presence of two and three adjoining thick brighter fringes (indicated by black arrows), suggesting locally different stacking vectors. In other words, subfamily A faults are present in 'subfamily B', tobelite-2M_2. The fact that most of the diffraction patterns taken along the [130] zone do not show the same degree of streaking as those acquired along [110], suggests that

https://doi.org/10.1180/minmag.2015.079.7.14 Published online by Cambridge University Press

TABLE 2. TEM-EDS analytical results of tobelite normalized on the basis of Si + Al + Fe + Mg = 6 atoms per formula unit.

	Sample 1										Sample 2			
	(1) All spots		(2) Highly faulted region		(3) Scarcely faulted region		(4) Dark contrast region		(5) Bright contrast region		(6) Region 1		(7) Region 2	
	Mean	Range	Mean	Range	Mean	Range	Mean	Range	Mean	Range	Mean	Range	Mean	Range
Na	0.44	0.26–0.81	0.31	0.29–0.33	0.53	0.37–0.81	0.37	0.33–0.40	0.31	0.28–0.33	0.33	0.25–0.64	0.19	0.14–0.40
Mg	0.33	0.25–0.55	0.32	0.30–0.33	0.42	0.34–0.55	0.34	0.32–0.36	0.31	0.28–0.34	0.29	0.23–0.36	0.00	0.00–0.01
Al	2.25	1.76–2.60	2.42	2.33–2.45	2.20	1.76–2.46	2.33	2.16–2.60	1.84	1.78–1.88	2.45	1.67–2.82	2.87	2.80–2.99
Si	3.41	3.03–3.93	3.25	3.20–3.34	3.36	3.15–3.67	3.30	3.03–3.47	3.84	3.78–3.93	3.25	2.86–4.09	3.09	2.98–3.18
K	0.04	0.00–0.15	0.08	0.04–0.15	0.04	0.00–0.09	0.04	0.01–0.07	0.02	0.02–0.03	0.07	0.01–0.19	0.17	0.13–0.22
Fe	0.02	0.00–0.03	0.02	0.01–0.02	0.02	0.01–0.03	0.02	0.01–0.03	0.01	0.00–0.01	0.01	0.00–0.02	0.03	0.02–0.05
Σ_{cat}	6.49	6.31–6.81	6.40	6.37–6.44	6.57	6.40–6.81	6.40	6.34–6.46	6.33	6.31–6.35	6.40	6.27–6.72	6.35	6.27–6.62

Notes: (1) average of 33 spot analyses on sample 1; (2) average of 7 spot analyses of a highly faulted zone (sample 1); (3) average of 3 spot analyses of an areas with a relatively low fault density (sample 1); (4) average of 4 spot analyses on a lamella with dark mass-thickness contrast (sample 1); (5) average of 3 spot analyses on an adjoining lamella with brighter mass-thickness contrast (sample 1); (6) average 17 spot analyses from region 1 sample 2; (7) average of 14 spot analyses from region 2 sample 2.

subfamily A faults are less frequent than subfamily B ones.

TEM microanalysis

The nanoscale chemical composition of the Armorican tobelite was investigated by EDS spectrometry in the TEM to ascertain the presence of any chemical heterogeneity and its relationship with microstructure. Compositional variability is found both between different TEM samples and within each sample from lamella to lamella, and sometimes within the same lamella.

Thirty-three spot analyses were measured on TEM sample 1 (see Table 2) in regions characterized by both abundance and paucity of faults, as well as by the occurrence of lamellae with different mass-thickness contrasts, in regions of virtually equal diffraction conditions and thicknesses (i.e. assuming that the different contrast was originated by a different composition). A total of thirty-one point analyses was, instead, collected on two regions of TEM sample 2 (see Table 2). No substantial chemical difference exists between the areas with high and low densities of stacking faults, but slight changes of Al/Si ratios and Na + K contents were detected. Analyses of regions of high concentration of stacking faults show slightly lower Si/Al (~1.3 *vs.* 1.5) and, correspondingly, lower Na + K content (~0.4 *vs.* 0.6 atoms per formula unit, a.p.f.u.) with respect to regions with low faults densities. The EDS data for lamellae with a bright mass-thickness contrast differ significantly from those acquired on the dark mass-thickness contrast lamellae of sample 1 for the highest Si/Al (~2.1 *vs.* 1.4) and lowest Na + K (~0.3 *vs.* 0.4 a.p.f.u.).

Concerning sample 2, slightly different average compositions have been observed in two regions. In particular, region 2 is characterized by different K and Na concentrations with respect to region 1 (K ≈ 0.17 *vs.* 0.07 and Na ≈ 0.19 *vs.* 0.33 a.p.f.u., respectively) and by the absence of Mg with respect to all the other measured EDS spot analyses.

In spite of the caution adopted during TEM-EDS measurements to avoid elemental diffusion (see Experimental section), ammonium could not be detected at significant levels in the samples studied. In order to trace the ammonium distribution within tobelite, we measured compositional profiles across tobelite lamellae at the SEM. The relatively lower accelerating voltage as compared to TEM-EDS (20 *vs.* 200 keV) and the acquisition time for each spot analyses (200 ms *vs.* 50 s), allowed us to detect, although qualitatively, ammonium.

https://doi.org/10.1180/minmag.2015.079.7.14 Published online by Cambridge University Press

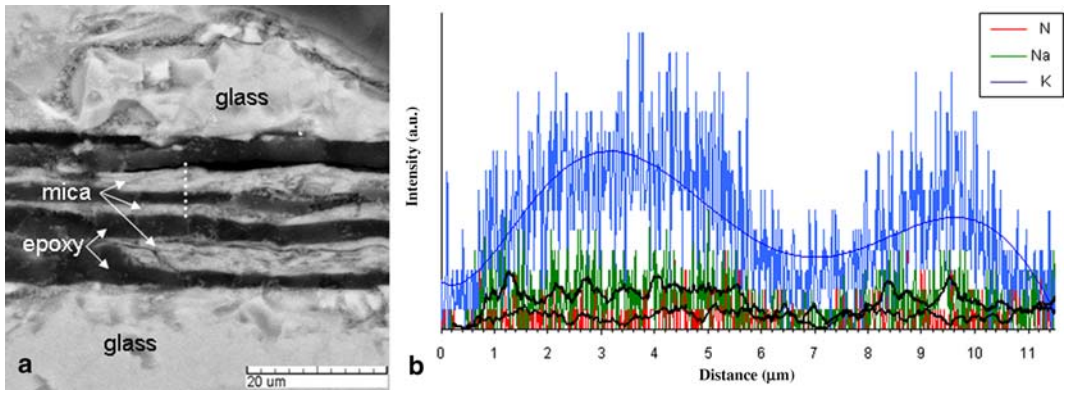


FIG. 9. (*a*) Back-scatter SEM image of a tobelite crystal embedded in epoxy resin and squeezed between two glass sections before ion milling for TEM observations. (*b*) EDS compositional profile along the dotted line reported in (*a*). The plot reports the Na-K and N-K intensities and the trace of the moving average over 15 spot analyses (total number of spots = 775 distributed over ~11.6 μm). The *K*α X-ray intensity is reported to help in localizing the centre of the two tobelite lamellae indicated by the profile: the maxima correspond to the centres of the lamellae, the minimum to epoxy. The graphs show a clear anti-correlation for Na and N.

The results are shown in Fig. 9. The traverse over which measurements were performed, ~11 μm long, is indicated by the dotted white line in Fig. 9*a*. The intensity concentration of K is reported to help in localizing the centre of the two tobelite lamellae indicated by the profile: as the interaction sphere of the electron beam is not fully confined within tobelite at the borders of the lamellae but affects the embedding epoxy, representative spot analyses are only those in the middle of the lamellae, corresponding to the maxima of the potassium signal. Because of the very short acquisition time for each spot analysis, the data are quite noisy, but sufficient to show that ammonium is correlated inversely with sodium.

Discussion and conclusions

The reconstruction of the stacking sequence in the Armorican tobelite has confirmed the 2M_2 polytype. At the same time, the occurrence of abundant stacking faults, both of subfamilies B and A have been detected, with apparent dominance of the former. However, in many cases, the actual stacking vector could not be worked out because of the rapid beam damage to the sample. As a further step, chemical analyses at the nanoscale were performed to try to correlate chemical features to stacking faults and/or to peculiar structural features revealed by single-crystal X-ray investigations (Mesto *et al.*, 2012).

It is known that the composition of tobelite may vary widely, in particular with reference to the K/NH_4^+ content. Tobelite studied by Higashi (1982) exhibited high NH_4^+ concentration (0.53 ammonium groups per formula units, g.p.f.u.); other natural ammonium-bearing micas with NH_4^+ contents up to 0.75 g.p.f.u. were also reported (Ruiz Cruz and Sanz de Galdeano, 2008). Several authors hypothesized a complete solid solution between tobelite and muscovite (Juster *et al.*, 1987; Wilson *et al.*, 1992; Drits *et al.*, 1997; Liang *et al.*, 1997), whereas Nieto (2002) showed that a miscibility gap between muscovite and tobelite may occur at temperatures <300°C.

Mesto *et al.* (2012) provided the following structural formulas based on bulk analyses: $(K_{0.18}Na_{0.01}(NH_4^+)_{0.62})_{\Sigma 0.81}(Al_{1.98}Fe^{3+}_{0.02})_{\Sigma 2.00}(Si_{3.19}Al_{0.81})_{\Sigma 4.00}O_{10.00}(OH)_{2.00}$ for their tobelite and $(K_{0.46}Na_{0.03}Ba_{0.01}(NH_4^+)_{0.36})_{\Sigma 0.86}(Al_{1.98}Mg_{0.01}Fe^{3+}_{0.01}V^{3+}_{0.01})_{\Sigma 2.00}(Si_{3.13}Al_{0.87})_{\Sigma 4.00}O_{10.00}(OH)_{1.92}$ for their NH_4^+-rich muscovite sample. Similar compositions were also reported on three spare crystals from the same suite as in Mesto *et al.* (2012) by Ottolini *et al.* (2014). In the latter case, the authors found significant N inhomogeneity by secondary ion mass spectrometry (SIMS).

In the present work, analyses of tobelite were obtained using the TEM-EDS within the Cliff-Lorimer approximation (Cliff and Lorimer, 1975) and using theoretical K-factors. Although this kind of analysis is not as accurate as electron microprobe

https://doi.org/10.1180/minmag.2015.079.7.14 Published online by Cambridge University Press

wavelength dispersive spectroscopic analyses and SIMS analyses, making any comparison difficult, the TEM analyses obtained are internally consistent and give provisional information about the compositional variability of tobelite at the nanoscale.

Summarizing, the composition of the tobelite samples studied by TEM may be described by three crystal chemical formulas:

$$(K_{0.06}Na_{0.39}(NH_4^+)_{0.55})_{\Sigma 1.00}(Al_{1.64}Mg_{0.34}Fe^{3+}_{0.02})_{\Sigma 2.00}(Si_{3.31}Al_{0.69})_{\Sigma 4.00}O_{10.00}(OH)_{2.00} \quad (1)$$

$$(K_{0.02}Na_{0.31}(NH_4^+)_{0.14})_{\Sigma 0.47}(Al_{1.68}Mg_{0.31}Fe^{3+}_{0.01})_{\Sigma 2.01}(Si_{3.84}Al_{0.16})_{\Sigma 4.00}O_{10.00}(OH)_{2.00} \quad (2)$$

$$(K_{0.17}Na_{0.19}(NH_4^+)_{0.58})_{\Sigma 0.94}(Al_{1.96}Fe^{3+}_{0.03})_{\Sigma 1.99}(Si_{3.09}Al_{0.91})_{\Sigma 4.00}O_{10.00}(OH)_{2.00} \quad (3)$$

calculated on the basis of 6 TOT cations (the total of Si, Al, Fe and Mg) and deriving the NH_4^+ content by charge balance considerations.

Formula 1 is representative of the average composition of the sample, being the average over the majority of the measured analytical points; Formula 2 describes the composition of the bright mass-thickness contrast lamellae; formula 3 represents the composition of region 2 of sample 2.

Note that compositional variations occur for nearly all elements, but particularly for the Si:Al and K:Na ratios and Mg concentration. According to our results, the estimated NH_4^+ and vacancy concentrations also point to notable changes, consistent with the results from the SIMS analyses (Ottolini *et al.*, 2014). We also note that formula 3, apart from the Na enrichment, approximates the bulk chemical composition obtained previously from electron microprobe analysis and structural data (Mesto *et al.*, 2012, see above).

However, formula 2, in comparison to formula 1 and 3, suggests an important loss of N and a high Si content, consistent with pyrophyllite-like substitution, a result in agreement with recent findings in ammonium muscovite samples (Ruiz Cruz, 2011). In this case, the decrease of the interlayer charge results in the drop of the electrostatic repulsion between the interlayer cations and the proton of the OH^- groups and, thus, in the reduction of the interlayer separation. However, it cannot be overlooked that the TEM analytical results indicate the constant presence of non-negligible Na concentration that was not detected at the bulk scale (see above).

As already reported in the Introduction section, Mesto *et al.* (2012) modelled the structural disorder in their NH_4^+-rich muscovite and the results were consistent with a shrinkage of the interlayer thickness, which was ascribed to the presence of a guest structure with a shorter *c* parameter than that of tobelite. No evidence of disorder involving lateral dimensions was found. The results of the TEM analysis here suggest that the ˙guest structure' in the tobelite may be associated with coherently-scattering domains having pyrophyllitic and/or paragonitic components (see formulas 1 and 2 above). Using structural data for pyrophyllite from Rayner and Brown (1966), i.e. $a = 5.17$, $b = 8.92$, $c = 18.66$ Å and $\beta = 99.8°$, it can be calculated that the pyrophyllite component should entail a $c \sin(\beta) \approx 18.38$ Å. Likewise, using data from Lin and Bailey (1984), i.e. $a = 5.128(2)$, $b = 8.898(3)$, $c = 19.287(9)$ Å and $\beta = 94.35(3)°$, it can be calculated that the paragonitic component in the tobelite structure should involve a $c \sin(\beta) \approx 19.24$ Å. Compared with the $c \sin(\beta)$ (~20.30 Å) of the tobelite in Mesto *et al.*, (2012), an average shortening of ~1.5 Å can be calculated which fits well the shrinkage (~1.3 Å) evaluated by those authors.

In conclusion, the heterogeneity revealed at the nanoscale attests to a change in mica chemistry, leading to silicon enrichment and to an emptying interlayer site together with an occurrence of relevant Na concentration. This circumstance may depend on changes in the chemical-physical constraints (lithological variations, fluid input flux, temperature, pressure, etc.) operating during and/or after tobelite formation (see the Occurrence section above).

Finally, no significant variation of the crystal chemistry was observed for regions with a high density of stacking faults with respect to the overall composition. This suggests that in tobelite the probability of the occurrence of faults with different operating stacking vectors may depend on formation conditions rather than crystal chemistry and that the faulting increases in an open system with rapid physicochemical changes which favour rapid growth of individual mica particles (Drits *et al.*, 2013).

Acknowledgements

This work was supported by the grants from the Italian Ministry of University and Research (MIUR). Thanks are due to Toshiro Kogure for critical reading of the manuscript and insightful suggestions. The

https://doi.org/10.1180/minmag.2015.079.7.14 Published online by Cambridge University Press

manuscript benefited from attentive reviews by Mark Welch and Richard Wirth.

References

Ahn, J.H., Peacor, D.R. and Essene, E.J. (1986) Cation-diffusion-induced characteristic beam damage in transmission electron microscope images of micas. *Ultramicroscopy*, **19**, 375–381.

Backhaus, K.O. and Ďurovič, S. (1984) Polytypism of micas; I, MDO polytypes and their derivation. *Clays and Clay Minerals*, **32**, 453–463.

Busigny, V. and Bebout, G.E. (2013) Nitrogen in the silicate Earth: Speciation and isotopic behavior during mineral-fluid interactions. *Elements*, **9**, 353–358.

Capitani, G.C., Oleynikov, P., Hovmöeller, S. and Mellini, M. (2006) A practical method to detect and correct for lens distortion in the TEM. *Ultramicroscopy*, **106**, 66–74.

Cliff, G. and Lorimer, G.W. (1975) The quantitative analysis of thin specimens. *Journal of Microscopy*, **103**(2), 203–207.

Drits, V.A., Lindgreen, H. and Salyn, A.L. (1997) Determination of the content and distribution of fixed ammonium in illite-smectite by X-ray diffraction: Application to North Sea illite-smectite. *American Mineralogist*, **82**, 79–87.

Drits, V.A., Sakharov, B.A., Ivanovskaya, T.A. and Pokrovskaya, E.V. (2013) Crystal-chemical micro-heterogeneity of Precambrian globular dioctahedral mica minerals. *Lithology and Mineral Resources,* **48** (6), 489–513.

Ďurovič, S., Weiss, Z. and Backhaus, K.-O. (1984) Polytypism of micas. II. Classification and abundance of MDO polytypes. *Clays and Clay Minerals*, **32**, 464–474.

Ferraris, G. and Ivaldi, G. (2002) Structural features of micas. Pp. 117–153 in: *Micas: Crystal Chemistry and Metamorphic Petrology* (A. Mottana, F.P. Sassi, J.B. Jr. Thompson and S. Guggenheim, editors). Reviews in Mineralogy and Geochemistry, **46**. Mineralogical Society of America and the Geochemical Society, Chantilly, Virginia.

Ferraris, G., Gula, A., Ivaldi, G., Nespolo, M., Sokolova, E., Uvarova, Y. and Khomyakov, A.P. (2001) First structure determination of an MDO-2*O* mica polytype associated with a 1*M* polytype. *European Journal of Mineralogy,* **13**(6), 1013–1023.

Fregola, R.A., Capitani, G.C., Scandale, E. and Ottolini, L. (2009) Chemical control of 3 *T* stacking order in a Li-poor biotite mica. *American Mineralogist*, **94**, 334–344.

Giuseppetti, G. and Tadini, C. (1972) The crystal structure of 2*O* brittle mica: anandite. *Tschermaks Mineralogische und Petrographische Mitteilungen*, **18**, 169–184.

Gloaguen, E., Branquet, Y., Boulvais, P., Moëlo, Y., Chauvel, J.-J., Chiappero, P.-J. and Marcoux, E. (2007) Paleozoic oolitic irestone of the French Armorican Massif: a chemical and structural trap for orogenic base metal-As-Sb-Au mineralisation during Hercynian strike-slip deformation. *Mineralium Deposita,* **42**(4), 399–422.

Harlov, D.E., Andrut, M. and Pöter, B. (2001) Characterisation of tobelite $(NH_4)Al_2[AlSi_3O_{10}](OH)_2$ and ND_4-tobelite $(ND_4)Al_2[AlSi_3O_{10}](OD)_2$ using IR spectroscopy and Rietveld refinement of XRD spectra. *Physics and Chemistry of Minerals*, **28**, 268–276.

Higashi, S. (1982) Tobelite, a new ammonium dioctahedral mica. *Mineralogical Journal*, **11**, 138–146.

Hovis, G.L., Harlov, D. and Gottshalk, M. (2004) Solution calorimetric determination of the enthalpies of formation of NH_4-bearing minerals buddingtonite and tobelite. *American Mineralogist*, **89**, 85–93.

Iijama, S. and Buseck, P.R. (1978) Experimental study of disordered mica structures by high-resolution electron microscopy. *Acta Crystallographica*, **A34**, 709–719.

Juster, T.C., Brown, P.E. and Bailey, S.W. (1987) NH_4-bearing illite in very low grade metamorphic rocks associated with coal, northeastern Pennsylvania. *American Mineralogist*, **72**, 555–565.

Kameda, J., Miyawaki, R., Drits, V.A. and Kogure, T. (2007) Polytype and morphological analyses of gümbelite, a fibrous Mg-rich illite. *Clays and Clay Minerals*, **55**, 453–466.

Kilaas, R. (1998) Optimal and near-optimal filters in high-resolution electron microscopy. *Journal of Microscopy*, **190**, 45–51.

Kogure, T. (2002) Investigations of micas using advanced transmission electron microscopy. Pp. 281–312 in: *Micas: Crystal Chemistry and Metamorphic Petrology* (A. Mottana, F.P. Sassi, J.B. Thompson Jr. and S. Guggenheim, editors). Reviews in Mineralogy and Geochemistry, **46**. Mineralogical Society of America, Chantilly, Virginia.

Kogure, T. (2013) Electron Microscopy. Pp. 275–317 in: *Handbook of Clay Science, second edition* (F. Bergaya and G. Lagaly, editors). Developments in clay science, 5. Elsevier.

Kogure, T. and Bunno, M. (2004) Investigation of polytypes in lepidolite using electron back-scattered diffraction. *American Mineralogist*, **89**, 1680–1684.

Kogure, T. and Nespolo, M. (1999*a*) First occurrence of a stacking sequence including (±60°, 180°) rotations in Mg-rich annite. *Clays and Clay Minerals*, **47**, 784–792.

Kogure, T. and Nespolo, M. (1999*b*) A TEM study of long-period mica polytypes: determination of the stacking sequence of oxybiotite by means of atomic resolution images and Periodic Intensity Distribution (PID). *Acta Cristallographica*, **B55**, 507–516.

https://doi.org/10.1180/minmag.2015.079.7.14 Published online by Cambridge University Press

Kogure, T., Kameda, J. and Drits, V.A. (2008) Stacking faults with 180° layer rotation in celadonite, an Fe- and Mg-rich dioctahedral mica. *Clays and Clay Minerals*, **56**, 612–621.

Levinson, A.A. (1953) Studies in the mica group; relationship between polymorphism and composition in the muscovite-lepidolite series. *American Mineralogist*, **38**, 88–107.

Liang, S., Ren, D., Wang, S. and Yao, G. (1997) Study of aluminium hydroxide minerals in tonsteins from Carbonifeous-permian coal-bearing series in nothern China. *Scienta Geologica Sinica*, **32**, 478–486.

Lin, C.-Y. and Bailey, S.W. (1984) The crystal structure of paragonite-2M_1. *American Mineralogist*, **69**, 122–127.

Mesto, E., Scordari, F., Lacalamita, L. and Schingaro, E. (2012) Tobelite and NH_4^+-rich muscovite single crystals from Ordovician Armorican sandstones (Brittany, France): Structure and crystal chemistry. *American Mineralogist*, **97**, 1460–1468.

Mitchell, D.R. (2007) HRTEM filter. Digital_Micrograph_Script_Database. http://felmpc14.tugraz.ac.at/dm_scripts/freeware/programs/hrtem_filter.htm.

Mugnaioli, E., Capitani, G.C., Nieto, F. and Mellini, M. (2009) Accurate and precise lattice parameters by selected-area electron diffraction in the transmission electron microscope. *American Mineralogist*, **94**, 793–800.

Nespolo, M. (1999) Analysis of family reflections of OD mica polytypes, and its application to twin identification. *Mineralogical Journal*, **21**, 53–85.

Nespolo, M (2001) Perturbative theory of mica polytypism. Role of the M2 layer in the formation of inhomogeneous polytypes. Clays and Clay Minerals, **49**, 1–23.

Ni, Y. and Hughes, J.M. (1996) The crystal structure of nanpingite-2M_2, the Cs end-member of muscovite. *American Mineralogist*, **81**, 105–110.

Nieto, F. (2002) Characterization of coexisting NH_4- and K-micas in very low-grade metapelites. *American Mineralogist*, **87**, 205–216.

Ottolini, L., Scordari, F. and Mesto, E. (2014) A new application of SIMS to the analysis of nitrogen in mica minerals: tobelite. *IOP Conference Series: Materials Science and Engineering*, **55**, 1–10.

Pöter, B., Gottschalk, M. and Heinrich, W. (2007) Crystal-chemistry of synthetic K-feldspar-buddingtonite and muscovite-tobelite solid solutions. *American Mineralogist*, **92**, 151–165.

Rayner, J.H. and Brown, G. (1966) Structure of pyrophyllite. *Clays and Clay Minerals*, **25**, 73–84.

Ruiz Cruz, M.D. (2011) NH_4-bearing micas in poly-metamorphic Alpujárride micaschists and gneisses from the central zone of the Betic Cordillera (Spain): tectono-metamorphic and crystal-chemical constraints. *Mineralogy and Petrology*, **101**, 225–244.

Ruiz Cruz, M.D. and Sanz de Galdeano, C. (2008) High-temperature ammonium white mica from the Betic Cordillera (Spain). *American Mineralogist*, **93**, 977–987.

Schreyer, W., Medenbach, O., Abraham, K., Gebert, W., Müller, W.F. (1982) Kulkeite, a new metamorphic phyllosilicate mineral: Ordered 1:1 chlorite/talc mixed-layer. *Contributions to Mineralogy and Petrology*, **80**, 103–109.

Shimoda, S. (1970) A hydromuscovite from the Shakanai Mine, Akita Prefecture, Japan. *Clays and Clay Minerals*, **18**, 269–274.

Smith, J.V. and Yoder, H.S. (1956) Experimental and theoretical studies of the mica polymorphs. *Mineralogical Magazine*, **31**, 209–235.

Takeda, H. and Ross, M. (1995) Mica polytypism: identification and origin. *American Mineralogist*, **80**, 715–724.

Tartese, R., Poujol, M., Gloaguen, E., Boulvais, P., Drost, K., Kosler, J. and Ntaflos, T. (2014) Hydrothermal activity during tectonic building of the Variscan orogen recorded by U-Pb systematic of xenotime in the Grès Armoricain formation, Massif Armoricain, France. *Mineralogy and Petrology*, **109**, 485–500.

Veblen, D.R. (1983*a*) Exsolution and crystal chemistry of the sodium mica wonesite. *American Mineralogist*, **68**, 554–565.

Veblen, D.R. (1983*b*) Microstructures and mixed layering in intergrown wonesite, chlorite, talc, biotite, and kaolinite. *American Mineralogist*, **68**, 566–580.

Wilson, P.N., Parry, W.T. and Nash, W.P. (1992) Characterization of hydrothermal tobelitic veins from black shale, Oquirrh Mountains, Utah. *Clays and Clay Minerals*, **40**, 405–420.

Zhoukhlistov, A.P., Zvyagin, B.B., Soboleva, S.V. and Fedotov, A.F. (1973) The crystal structure of the dioctahedral mica 2M_2 determined by high voltage electron diffraction. *Clays and Clay Minerals*, **21**, 465–470.

Zvyagin, B.B. (1988) Polytypism of crystal structures. *Computers and Mathematics with Applications*, **16**, 569–591.

https://doi.org/10.1180/minmag.2015.079.7.14 Published online by Cambridge University Press